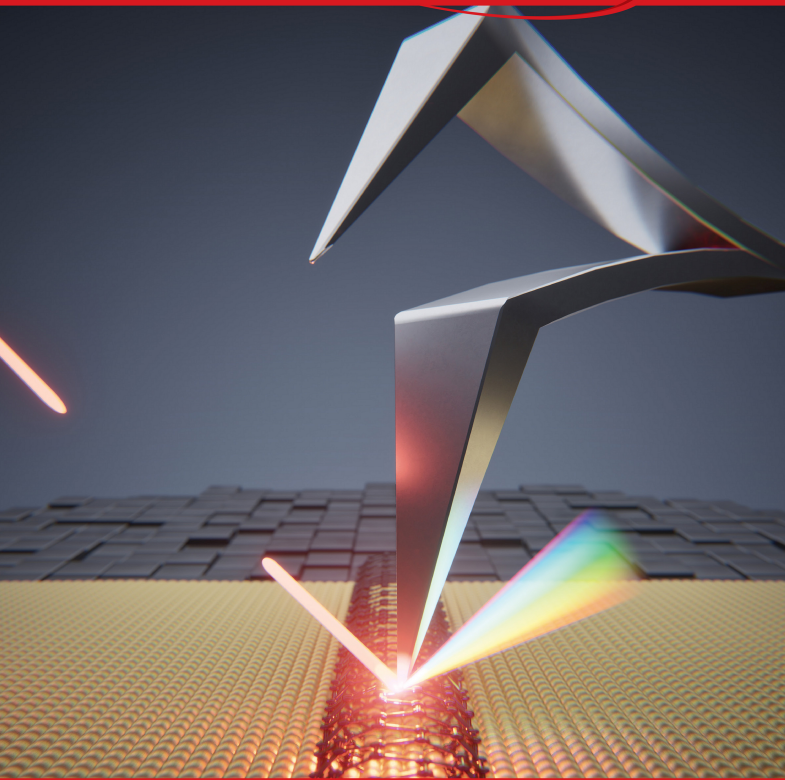


NANO LETTERS

April 9, 2025
Volume 25, Number 14
pubs.acs.org/NanoLett



ACS Publications
Most Trusted. Most Cited. Most Read.

www.acs.org

Modulated-Illumination Intermittent-Contact Tip-Enhanced Raman Spectroscopy

Michael G. Ruppert,* Ben S. Routley, Luke R. McCourt, Yuen K. Yong, and Andrew J. Fleming



Cite This: *Nano Lett.* 2025, 25, 5656–5662



Read Online

ACCESS |



Metrics & More



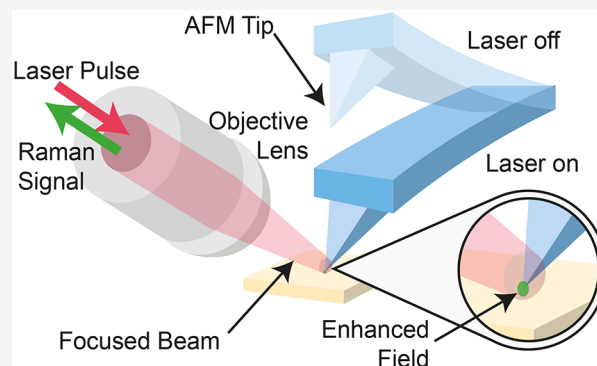
Article Recommendations



Supporting Information

ABSTRACT: This article presents a proof-of-concept for a new imaging method that combines tip-enhanced Raman spectroscopy with intermittent-contact atomic force microscopy to provide simultaneous nanometer-scale mechanical force imaging with chemical contrast. The foremost difference from a standard tip-enhanced Raman microscope is the Raman illumination, which is modulated by the cantilever drive signal so that illumination is only active when the tip is close to the surface. This approach significantly reduces contact forces and thermal damage due to constant illumination while simultaneously reducing background Raman signals. Near-field optical and dynamic cantilever simulations highlight the effect of the imaging parameters on the tip–sample force and the evanescent field enhancement. The experimental images obtained with this new imaging method demonstrate a lateral resolution sufficient to identify single-walled carbon nanotube bundles with a full width at half-maximum of 20 nm.

KEYWORDS: *Tip-Enhanced Raman Spectroscopy (TERS), Dynamic-mode Atomic Force Microscopy (AFM), Carbon Nanotubes (CNT), Laser Modulation*



Tip-enhanced Raman spectroscopy (TERS) combines the chemical sensitivity of Raman spectroscopy with the subdiffraction-limited resolution of near-field optics.^{1–6} TERS has become established as a powerful imaging tool with reports of spatial resolutions as low as 1–15 nm under ambient conditions^{7–13} and sub-nanometer spatial resolution under ultrahigh vacuum and cryogenic temperatures.^{14–16} TERS relies on the formation of localized surface plasmons at the end of a metal probe.^{11,17–19} Since the intensity and spatial confinement of this evanescent field decays exponentially with increasing tip–sample distance,^{12,20} atomic force microscopy (AFM) feedback techniques are conventionally employed to maintain the separation.⁶

There are three typical optical configurations used for TERS: top illumination and collection; side illumination and collection; and bottom illumination and collection.¹ If the sample is transparent, bottom illumination and collection can be used, allowing for the illumination beam to be focused through the sample onto the tip apex.¹⁸ For opaque samples, top illumination and collection²¹ is required to avoid cantilever shadowing; a specialized tilted TERS probe is needed. Finally, the side illumination and collection configuration²² is suited to opaque samples and allows an optimal polarization alignment with the probe tip, while reducing direct back scatter. This mode requires a focusing lens with a high numerical aperture (NA) and a long working distance, but parabolic focusing mirrors can be used as an alternative.^{23,24}

Conventional TERS, based on contact mode AFM feedback, is routinely used for spectroscopy of single points; however, simultaneous recording of topographic maps and Raman spectra in contact mode is complicated by several factors, including the effect of contact forces, which can cause critical deformations and displacements²⁵ when imaging soft, sticky, or easily displaced samples. Thermal damage can also occur due to constant laser exposure.⁶ To reduce contact forces, dynamic AFM methods such as tapping-mode AFM²⁶ are required to widen the application range of AFM-TERS imaging. This combination has also been adopted in other near-field spectroscopy applications, such as infrared spectroscopy (AFM-IR).²⁷

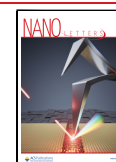
In order to reduce damage to the sample and tip during topography acquisition, a hybrid mode between contact mode TERS and intermittent contact mode AFM was demonstrated for imaging functional groups on the surface of two-dimensional materials.²⁸ In this mode, the *z*-axis feedback is switched between the constant-force contact mode for Raman

Received: December 13, 2024

Revised: March 4, 2025

Accepted: March 5, 2025

Published: March 13, 2025



spectra acquisition and constant-amplitude intermittent-contact mode for topography acquisition. In practice, this mode is inherently slow and the switching between feedback parameters leads to artifacts in the topography channel, as shown in Figure 3(B).

The disadvantages associated with contact-mode TERS have led to the development of TERS modes purely based on intermittent-contact-mode AFM.^{12,20,29–35} In these modes, the AFM is operated continuously in constant-amplitude intermittent-contact mode with continuous or gated illumination and collection of Raman spectra. The combination of TERS and intermittent-contact mode inherits the benefits of reduced lateral friction and reduced adhesion for soft samples, while maintaining high resolution in the z -direction.^{36,37} However, the intensity and spatial confinement of the evanescent field will decay exponentially with distance from the probe,^{12,20} which requires precise control and timing between the tip–sample distance and spectrum acquisition. This can be achieved by temporal gating of the Raman spectra detection system.^{20,30} To be effective, the gating needs to occur for a fraction of the probe cycle time, on the order of a few hundred nanoseconds.²⁰ Since the response time of charge-coupled device array-based spectrometers is insufficient for these timing requirements, avalanche photodiode arrays have been used to gate the Raman acquisition.²⁰ In this approach, the ability to measure multiple Raman bands is sacrificed to enable precise gating at the expense of reducing the Raman spectra to a single band. These snapshots can then be used to estimate the background Raman signal which is removed from the final measurement.^{20,30} Another disadvantage is that the cantilever tip and sample experience continuous laser exposure, while the Raman acquisition is confined to a small fraction of the cantilever oscillation cycle, potentially leading to degradation of the tip and delicate samples.

An alternative to gated acquisition is to modulate the Raman laser illumination beam.¹² Advantageously, this method uses a standard spectrometer that acquires multiple bands simultaneously. The concept of this technique is illustrated in Figure 1, which shows the illumination laser being pulsed when the probe is in contact with the sample and highlights the duty cycle as an important parameter. This technique was first experimentally investigated by Kawata et al.,¹² who used precise tip–sample distance control to profile the spatial decay of the evanescent field forming at the end of the tip. In their work, multiple Raman measurements are taken along an isolated single-walled carbon nanotube; however, no complete Raman images or height maps are reported.

In this article, we present a complete proof-of-concept for a new imaging mode termed modulated-illumination intermittent-contact TERS (MIIC-TERS) with the ability to acquire intermittent-contact AFM topography images and full-spectrum TERS images simultaneously. The modulation scheme significantly reduces the background Raman signal compared to intermittent-contact AFM modes with constant illumination and inherits low tip–sample interaction forces from tapping-mode AFM. The MIIC-TERS imaging mode is experimentally compared to constant-illumination intermittent-contact TERS (CIIC-TERS) and a recently developed hybrid mode.^{28,38} Additionally, near-field optical simulations coupled with dynamic cantilever simulations are used to examine the influence of AFM imaging parameters and the TERS duty cycle on the tip–sample force and evanescent field enhancement.

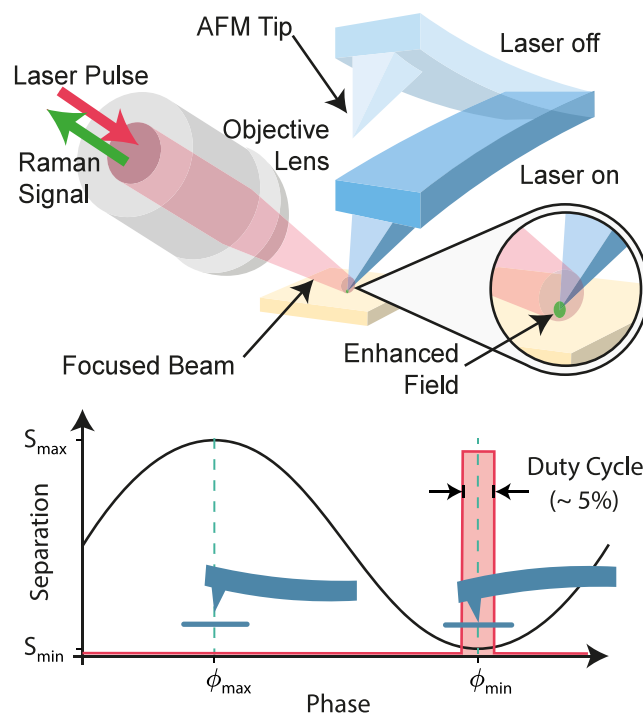


Figure 1. Schematic representation of MIIC-TERS. The Raman laser is synchronized with the cantilever deflection to allow precise timing of the laser modulation with respect to the AFM cantilever position.

The experimental setup is based on a modified Horiba XploRA-AFM TERS microscope, as described in Figure 2. An acoustic optical modulator (AOM) modulates the illumination source. The Raman laser exposure time is kept constant at 500 ms for all imaging modes, and the sample scanner is held constant during laser exposure at each pixel, which leads to a slightly longer pixel dwell time. For hybrid mode TERS, the pixel dwell time must be increased further to accommodate the tip–sample approach and retraction time and to allow for settling of the cantilever dynamics, which leads to a longer overall imaging time. A detailed description of the imaging protocols and parameters for the hybrid mode, CIIC-TERS, and MIIC-TERS are listed in the Supporting Information.

Normalized G-band maps and height images of graphene flakes using hybrid mode TERS and CIIC-TERS are shown in Figure 3. Although hybrid mode TERS provides an acceptable Raman map in Figure 3(A), the height map in Figure 3(B) exhibits the line artifacts labeled A and area artifacts labeled B. In contrast, the Raman map obtained with CIIC-TERS in Figure 3(C) appears noisy due to the low number of counts, which are plotted in Figure 3(E). Figure 3(E) also shows that the CIIC-TERS background signal is similar to the hybrid mode, but the Raman signal is much lower, which is due to the small percentage of time that the probe tip is near the sample. Although the CIIC-TERS Raman map is noisy, the height map in Figure 3(D) is free from artifacts associated with surface tracking, e.g., artifacts such as features A and B in Figure 3(B). An investigation of the area artifacts in Figure 3(B) found that the hybrid mode to-contact procedure, which is required at each pixel, does not result in identical force and amplitude set points for consecutive pixels when switching between tapping mode and contact mode on flat areas of the sample, and therefore, the resulting amplitude of the cantilever deflection is

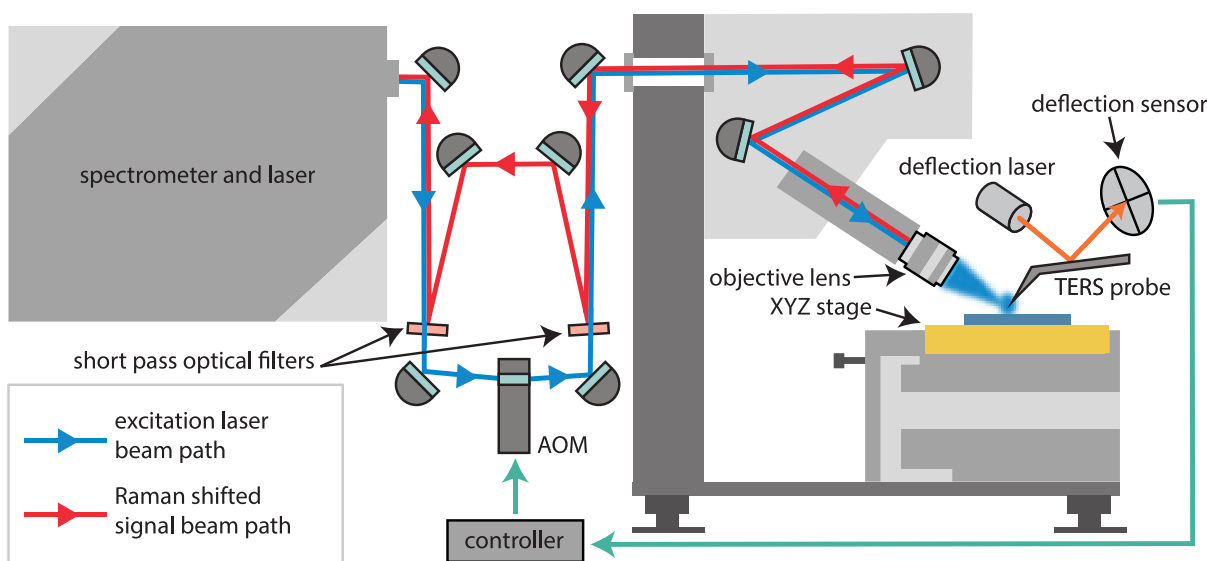


Figure 2. Schematic of the MIIC-TERS experimental setup. The custom-built free-space optical modulation system includes a laser source and spectrometer (Horiba XploRA-AFM TERS microscope), an acoustic optical modulator (Isomet IMAD-P80L-1.5), two optical edge filters (Semrock 638 nm), alignment, and bypass mirrors.

not purely a function of the topography and can lead to imaging artifacts.

These experiments demonstrate that the hybrid mode provides adequate Raman mapping at the expense of high contact forces and low-quality topographic imaging. Conversely, CIIC-TERS provides low contact forces and high-quality topographic imaging at the expense of low-quality Raman mapping. Therefore, there is a significant need for a combination of high-quality Raman and topographic imaging with low contact forces, which is achieved by the proposed modulated-illumination intermittent-contact mode.

A time-domain simulation of the TERS probe trajectory was combined with a stationary optical model to investigate the effect of the laser pulse timing. The trajectory simulation was used to determine the probe's separation as a function of time, which can be seen in Figure 4(B), along with the relative instantaneous tip-sample force. Subsequently, the optical model in Figure 4(A) is applied for a given probe separation to yield relative electric field enhancement. The model stipulates that the electric field decays exponentially with tip-sample distance which agrees with recent experimental findings.³⁰ By combination of these models, the relative electric field enhancement as a function of time is plotted in Figure 4(B). The dynamic simulation does not allow for sample indentation during repulsive interaction which causes a zero tip-sample distance and maximum electric field enhancement for multiple points in time. Figure 4(C) shows the average relative electric field enhancement as a function of the laser pulse duty cycle for different amplitude set points. For a duty cycle of 100% and amplitude set point of 75%, which is the case for the experimental CIIC-TERS results presented thus far, the average relative electric field enhancement (Raman signal to background ratio) is approximately 0.3 and hence explains the poor experimental Raman measurement for this mode.

The simulation results in Figure 4(C) suggest that a lower duty cycle is always desirable to increase the average relative electric field enhancement, but this conclusion neglects noise sources present in the spectrometers. For a constant integration and imaging time, a lower duty cycle will reduce

the overall signal integrated by the spectrometer leading to lower signal-to-noise ratio. This can be counteracted by increasing the integration time, however, at the expense of image acquisition time. An alternative approach is to decrease the AFM amplitude set point, as demonstrated in Figure 4(C), allowing for a longer duty cycle for a given relative electric field enhancement. However, decreasing the amplitude set point will increase the tip-sample forces³⁹ which may lead to damage of the sample and tip. Additionally, for high set points, the cantilever may remain in the attractive imaging regime⁴⁰ which limits the minimum tip-sample distance, resulting in a reduced relative electric field enhancement, even for low duty cycles. Ultimately, the laser duty cycle and AFM amplitude set point need to be tuned for a given cantilever and sample combination to achieve the desired balance of relative electric field enhancement, tip-sample force interaction, and imaging time.

To demonstrate the imaging capabilities of MIIC-TERS, high-resolution Raman and topography maps were collected simultaneously from carbon nanotubes and graphene flakes. Figure 5 shows the Raman maps and topography of a carbon nanotube cluster with a 10 nm pixel size.

Figure 5(E) shows the Raman spectra for the three points highlighted in Figure 5(A)-(C). The Raman spectra for point 1 show high counts for the D-band (1350 cm^{-1}) and G-band (1580 cm^{-1}) with a lower count for the 2D-band (2680 cm^{-1}). These spectral properties, combined with the size of the features, lead to the conclusion that point 1 corresponds to a multiwalled carbon nanotube.⁴¹ Similarly, the cross section P*-P of a multiwalled carbon nanotube shown in Figure 5(F) highlights the subdiffraction limited resolution with a full-width at half-maximum of approximately 20 nm. Point 2 has a high count for the G- and 2D-bands and a low count for the D-band. Given its shape and size in conjunction with these spectral properties, it is concluded that this point corresponds to a multilayered graphene flake.⁴² Point 3 shows a high count only for the G-band, and given its small width, it can be concluded that it corresponds to a single-walled carbon nanotube.⁶

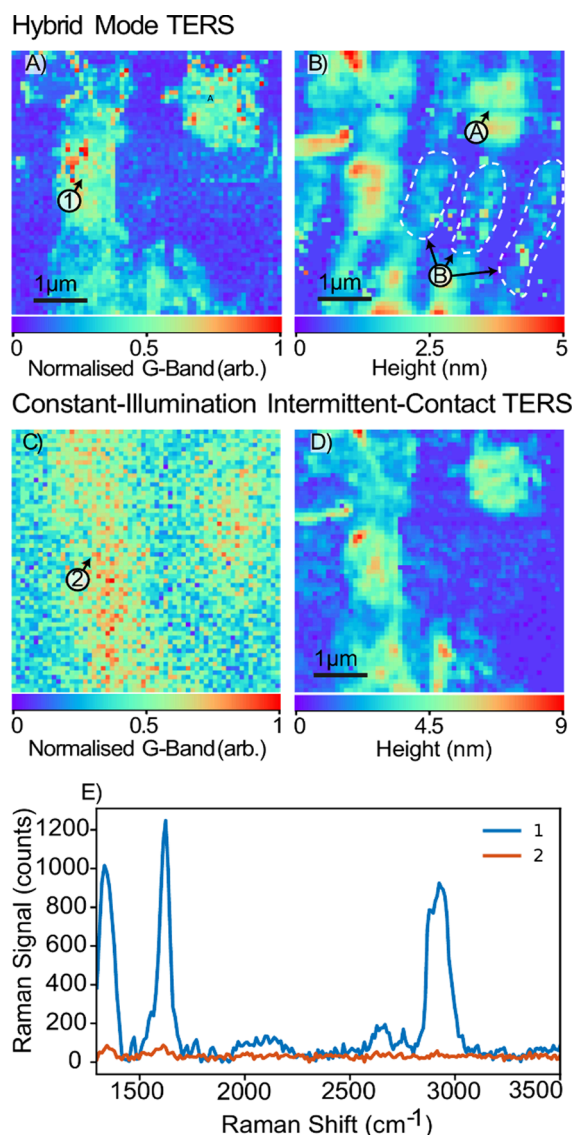


Figure 3. Experimental verification of hybrid mode TERS and CIIC-TERS. (A) G-band (1580 cm^{-1}) Raman map and (B) height map using hybrid mode TERS; Topography artifacts are highlighted with labels A and B. (C) G-band Raman map and (D) height map by using CIIC-TERS. (E) Raman spectra of the points labeled 1 and 2 in (A) and (C). Imaging parameters: Free-air amplitude 20 nm ; amplitude set point 55% (hybrid), 35% (CIIC); image size $5 \times 5\ \mu\text{m}$, 100×100 pixel; pixel dwell time 700 ms (hybrid), 600 ms (CIIC); exposure time 500 ms ; imaging time 117 min (hybrid), 100 min (CIIC).

Figure 5(C), (D) show images of the G-band Raman signal and the topography. The only common feature in both of these maps is the graphene flake. Due to the large 200 nm probe radius, the topography resolution is insufficient to resolve the multiwall and single-wall carbon nanotubes labeled 1 and 2; that is, MIIC-TERS provides better spatial resolution in the Raman map compared to the topography map.

It can be observed that the Raman maps and topography map are free from artifacts associated with AFM feedback errors, such as line artifacts or other discontinuities. The topography map in Figure 5(D) reveals two large round features in the top-right and lower-left corner which are not represented in the corresponding TERS images. In particular, the feature in the top-right corner shadows the graphene flake

2 which is highlighted with arrows in Figure 5(A)–(C). Since these features do not exhibit any significant Raman spectra, it is assumed they are due to sample contamination which introduces an approximately 12 nm offset between the TERS probe tip and sample surface, resulting in significant enhancement reduction according to Figure 4(A). Further analysis is provided in the Supporting Information.

Figure 5(G) shows an offset between the Raman signal and the topography, which is estimated to be 30 nm . This offset is caused by the random granular nature of the silver probe coating. When silver is evaporated onto a SiO_2 probe, the difference in surface free energy leads to the formation of a granular silver layer and the near-field enhancement is concentrated around these grains.^{42–44} As a result, if the grain responsible for the Raman signal is different from the grain making contact with the sample, an offset between the topography and Raman image can be observed.⁴⁵ Assuming the two grains are adjacent to each other, the grain size is equal to the offset of 30 nm , which is in good agreement with reported values of 40 nm for a similar probe.⁴²

The AFM-TERS imaging results presented in this article were acquired with different silver-coated TERS probes and in different regions on the sample. This approach was required due to the short lifetime of silver AFM-TERS probes.^{42–45} Consequently, imaging parameters such as the amplitude set point, Raman hot spot on the tip apex, MIIC-TERS phase offset, and MIIC-TERS duty cycle must be optimized for each TERS probe and imaging mode. Due to the variability between probes,⁴⁶ direct comparisons between the Raman signal-to-noise ratio of each imaging mode is challenging.

All AFM-TERS results presented in this work were acquired on gold substrates, which can result in stronger electric-field enhancement of the combined substrate-sample-tip system.^{47,48} Since all imaging modes were tested on the same sample, the bias introduced through additional enhancement from the gold substrate is common for all imaging modes and is not expected to influence the comparisons or conclusions.

The article demonstrates tip-enhanced Raman spectroscopy using intermittent contact and modulated illumination to provide low contact forces and simultaneous high-quality Raman and topographic imaging. The mode is experimentally compared to a recently published hybrid mode and intermittent-contact TERS with constant illumination. The results verify the need for accurate timing between Raman acquisition and tip–sample separation to maximize the signal-to-background ratio. The results are consistent with near-field optical simulations that predict improved average enhancement with a reduced illumination duty cycle.

While all three imaging modes were tested with equivalent Raman laser exposure times of 500 ms , MIIC-TERS would benefit from extended pixel integration times to increase the overall signal-to-background ratio at the expense of imaging time. However, due to thermal drift of the custom free-space optical modulation system, longer integration times are prohibitive particularly at ambient temperatures.⁴⁹ In the future, the authors aim to fiber-couple the optical modulation system to significantly reduce optical drift which would allow longer pixel integration times. Another significant barrier is the poor yield, high cost, low reproducibility, and short lifetime of silver-coated TERS probes.^{6,27,50} These limitations make it challenging to objectively compare the Raman signal-to-background ratio for different AFM-TERS imaging modes, particularly when multiple TERS probes must be employed.

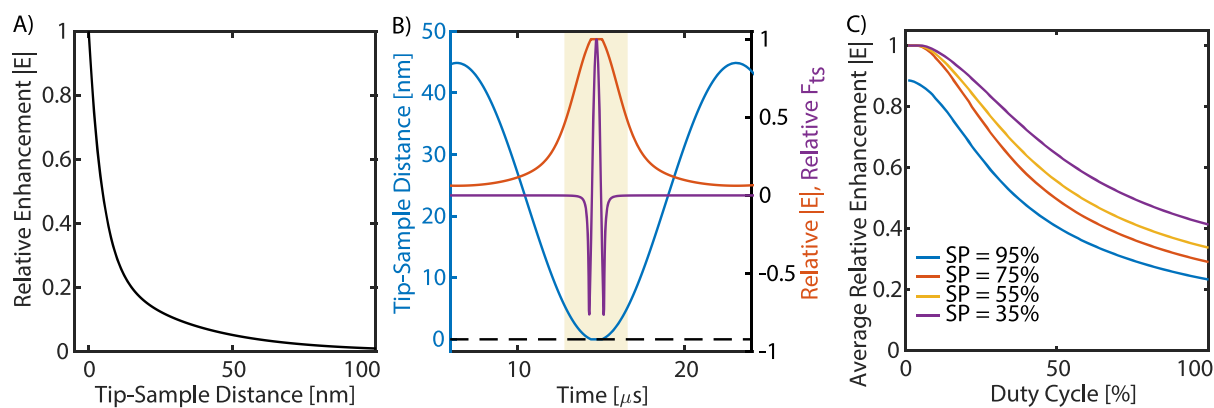


Figure 4. Near-field optical and dynamic cantilever simulations to study the effect of the AFM imaging parameters and TERS duty cycle on the tip–sample force and evanescent field enhancement. (A) Stationary optical model for the relative near-field enhancement as a function of tip–sample separation. (B) Time-domain simulation of the cantilever tip trajectory during intermittent-contact mode, relative tip–sample force F_{ts} , and resulting relative near-field enhancement $|E|$ (the highlighted area represents the definition of the duty cycle). (C) Average relative enhancement as a function of duty cycle for different amplitude set points.

Modulated-Illumination Intermittent-Contact TERS

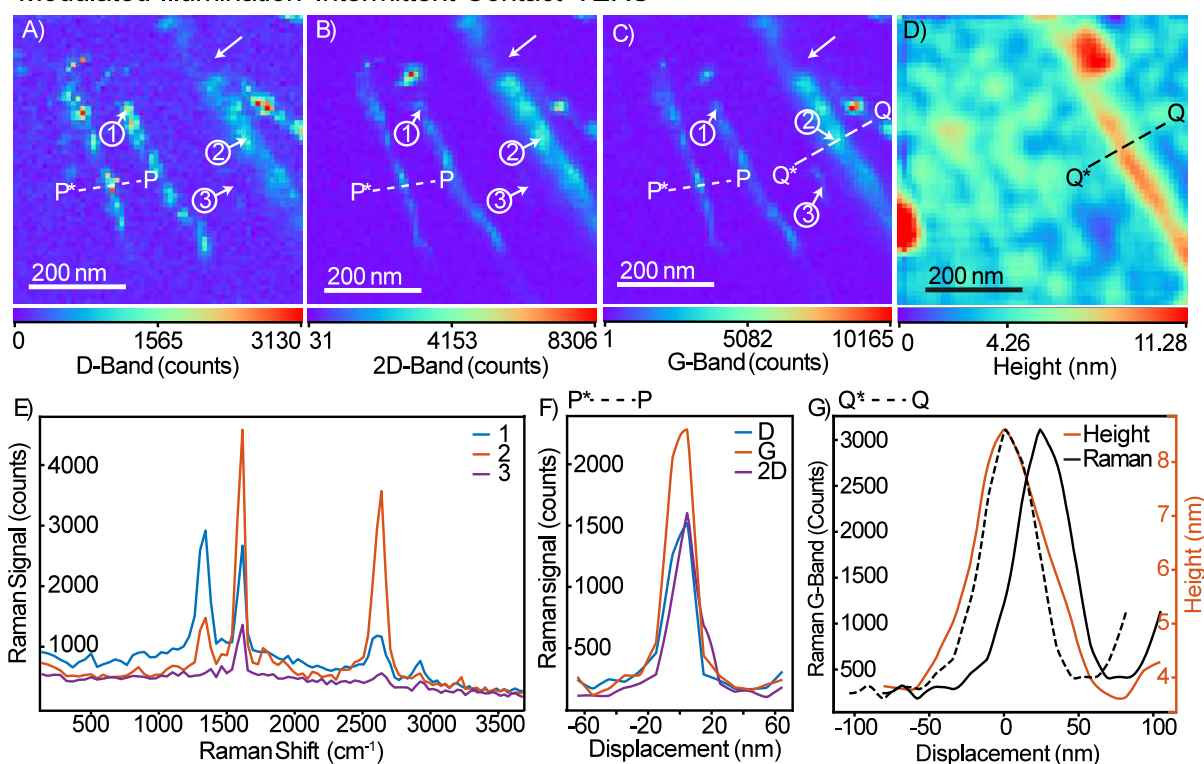


Figure 5. Experimental verification of MIIC-TERS. (A) D-band (1350 cm^{-1}) Raman map, (B) 2D-band (2680 cm^{-1}) Raman map, (C) G-band (1580 cm^{-1}) Raman map, (D) intermittent contact AFM height map, (E) Raman spectrum of the points highlighted in (A)–(C), (F) Raman D-, 2D-, and G-bands for the cross section P*–P highlighted in (A)–(C), and (G) Raman G-band and height for the cross section Q*–Q highlighted in (C), (D). The dashed line represents the Raman cross section shifted by an offset of 30 nm. Imaging parameters: Free-air amplitude 20 nm; amplitude set point 46%; image size $1 \times 1\ \mu\text{m}$, 100×100 pixel; pixel dwell time 600 ms; exposure time 500 ms; duty cycle 5%; imaging time 100 min. The images in (A)–(D) have been cropped.

Promising candidates to alleviate these problems are gold nanocone probes^{43,45} which offer superior lifetime, and collocation of the mechanical tip apex and optical hot-spot, at the expense of lower enhancement compared to silver tips. Optimizing the fabrication of such tips remains an active research area.⁴⁵

ASSOCIATED CONTENT

Data Availability Statement

All relevant data are displayed within the manuscript and its Supporting Information.

Supporting Information

The Supporting Information is available free of charge at <https://pubs.acs.org/doi/10.1021/acs.nanolett.4c06397>.

Detailed description of the imaging protocols and parameters for hybrid mode TERS, CIIC-TERS, and MIIC-TERS as well as more details on the numerical modeling. Additional analysis on the shadowing feature observed in Figure 5(D) (PDF)

AUTHOR INFORMATION

Corresponding Author

Michael G. Ruppert – University of Technology Sydney,
Centre for Audio, Acoustics and Vibration, Ultimo, NSW
2007, Australia; orcid.org/0000-0003-2286-4929;
Email: michael.ruppert@uts.edu.au

Authors

Ben S. Routley – The University of Newcastle, Callaghan,
NSW 2308, Australia

Luke R. McCourt – The University of Newcastle, Callaghan,
NSW 2308, Australia; orcid.org/0000-0003-0593-6054

Yuen K. Yong – The University of Newcastle, Callaghan,
NSW 2308, Australia

Andrew J. Fleming – The University of Newcastle, Callaghan,
NSW 2308, Australia

Complete contact information is available at:

<https://pubs.acs.org/10.1021/acs.nanolett.4c06397>

Author Contributions

M.G.R. and B.S.R. contributed equally to this work. B.S.R. and M.G.R. performed TERS experiments, analyzed the data, and wrote the manuscript. B.S.R. built the experimental optomechanical setup. M.G.R. and L.R.M. performed the simulations. M.G.R. and A.J.F. conceived the idea and planned the experiments. All authors contributed to discussions of the results.

Notes

The authors declare no competing financial interest.

ACKNOWLEDGMENTS

M.G.R. is the recipient of an Australian Research Council Discovery Early Career Award (DE240100507) funded by the Australian Government. This project was further supported by the Australian Research Council grants LE160100234, DP170101813, and DP210103383.

REFERENCES

- (1) Stadler, J.; Schmid, T.; Zenobi, R. Developments in and practical guidelines for tip-enhanced Raman spectroscopy. *Nanoscale* **2012**, *4*, 1856–1870.
- (2) Schmid, T.; Opilik, L.; Blum, C.; Zenobi, R. Nanoscale Chemical Imaging Using Tip-Enhanced Raman Spectroscopy: A Critical Review. *Angew. Chem., Int. Ed.* **2013**, *52*, 5940–5954.
- (3) Fujita, Y.; Walke, P.; De Feyter, S.; Uji-i, H. Tip-enhanced Raman scattering microscopy: Recent advance in tip production. *Jpn. J. Appl. Phys.* **2016**, *55*, No. 08NA02.
- (4) Deckert-Gaudig, T.; Taguchi, A.; Kawata, S.; Deckert, V. Tip-enhanced Raman spectroscopy from early developments to recent advances. *Chem. Soc. Rev.* **2017**, *46*, 4077–4110.
- (5) Shao, F.; Zenobi, R. Tip-enhanced Raman spectroscopy: principles, practice, and applications to nanospectroscopic imaging of 2D materials. *Anal. Bioanal. Chem.* **2019**, *411*, 37–61.
- (6) Verma, P. Tip-Enhanced Raman Spectroscopy: Technique and Recent Advances. *Chem. Rev.* **2017**, *117*, 6447–6466.
- (7) Treffer, R.; Lin, X.; Bailo, E.; Deckert-Gaudig, T.; Deckert, V. Distinction of nucleobases - a tip-enhanced Raman approach. *Beilstein Journal of Nanotechnology* **2011**, *2*, 628–637.
- (8) Stadler, J.; Schmid, T.; Zenobi, R. Nanoscale Chemical Imaging of Single-Layer Graphene. *ACS Nano* **2011**, *5*, 8442–8448.
- (9) Yano, T.-a.; Verma, P.; Saito, Y.; Ichimura, T.; Kawata, S. Pressure-assisted tip-enhanced Raman imaging at a resolution of a few nanometres. *Nat. Photonics* **2009**, *3*, 473–477.
- (10) Steidtner, J.; Pettinger, B. Tip-Enhanced Raman Spectroscopy and Microscopy on Single Dye Molecules with 15 nm Resolution. *Phys. Rev. Lett.* **2008**, *100*, No. 236101.
- (11) Anderson, N.; Hartschuh, A.; Cronin, S.; Novotny, L. Nanoscale Vibrational Analysis of Single-Walled Carbon Nanotubes. *J. Am. Chem. Soc.* **2005**, *127*, 2533–2537.
- (12) Ichimura, T.; Fujii, S.; Verma, P.; Yano, T.; Inouye, Y.; Kawata, S. Subnanometric Near-Field Raman Investigation in the Vicinity of a Metallic Nanostructure. *Phys. Rev. Lett.* **2009**, *102*, No. 186101.
- (13) He, Z.; Han, Z.; Kizer, M.; Linhardt, R. J.; Wang, X.; Sinyukov, A. M.; Wang, J.; Deckert, V.; Sokolov, A. V.; Hu, J.; et al. Tip-enhanced Raman imaging of single-stranded DNA with single base resolution. *J. Am. Chem. Soc.* **2019**, *141*, 753–757.
- (14) Zhang, R.; Zhang, Y.; Dong, Z.; Jiang, S.; Zhang, C.; Chen, L.; Zhang, L.; Liao, Y.; Aizpurua, J.; Luo, Y. e.; et al. Chemical mapping of a single molecule by plasmon-enhanced Raman scattering. *Nature* **2013**, *498*, 82–86.
- (15) Zhang, Y.; Yang, B.; Ghafoor, A.; Zhang, Y.; Zhang, Y.-F.; Wang, R.-P.; Yang, J.-L.; Luo, Y.; Dong, Z.-C.; Hou, J. G. Visually constructing the chemical structure of a single molecule by scanning Raman picoscopy. *National Science Review* **2019**, *6*, 1169–1175.
- (16) Lee, J.; Crampton, K. T.; Tallarida, N.; Apkarian, V. A. Visualizing vibrational normal modes of a single molecule with atomically confined light. *Nature* **2019**, *568*, 78–82.
- (17) Hayazawa, N.; Inouye, Y.; Sekkat, Z.; Kawata, S. Metallized tip amplification of near-field Raman scattering. *Opt. Commun.* **2000**, *183*, 333–336.
- (18) Stöckle, R. M.; Suh, Y. D.; Deckert, V.; Zenobi, R. Nanoscale chemical analysis by tip-enhanced Raman spectroscopy. *Chem. Phys. Lett.* **2000**, *318*, 131–136.
- (19) Neacsu, C. C.; Dreyer, J.; Behr, N.; Raschke, M. B. Scanning-probe Raman spectroscopy with single-molecule sensitivity. *Phys. Rev. B* **2006**, *73*, No. 193406.
- (20) Yu, J.; Saito, Y.; Ichimura, T.; Kawata, S.; Verma, P. Far-field free tapping-mode tip-enhanced Raman microscopy. *Appl. Phys. Lett.* **2013**, *102*, 123110.
- (21) Stadler, J.; Schmid, T.; Zenobi, R. Nanoscale Chemical Imaging Using Top-Illumination Tip-Enhanced Raman Spectroscopy. *Nano Lett.* **2010**, *10*, 4514–4520.
- (22) Nieman, L. T.; Krampert, G. M.; Martinez, R. E. An apertureless near-field scanning optical microscope and its application to surface-enhanced Raman spectroscopy and multiphoton fluorescence imaging. *Rev. Sci. Instrum.* **2001**, *72*, 1691–1699.
- (23) Klingsporn, J. M.; Jiang, N.; Pozzi, E. A.; Sonntag, M. D.; Chulhai, D.; Seideman, T.; Jensen, L.; Hersam, M. C.; Duyne, R. P. V. Intramolecular Insight into Adsorbate-Substrate Interactions via Low-Temperature, Ultrahigh-Vacuum Tip-Enhanced Raman Spectroscopy. *J. Am. Chem. Soc.* **2014**, *136*, 3881–3887.
- (24) Zhang, D.; Wang, X.; Braun, K.; Egelhaaf, H.-J.; Fleischer, M.; Hennemann, L.; Hintz, H.; Stanciu, C.; Brabec, C. J.; Kern, D. P.; Meixner, A. J. Parabolic mirror-assisted tip-enhanced spectroscopic imaging for non-transparent materials. *J. Raman Spectrosc.* **2009**, *40*, 1371–1376.
- (25) Yano, T.-a.; Ichimura, T.; Kuwahara, S.; H'Dhili, F.; Uetsuki, K.; Okuno, Y.; Verma, P.; Kawata, S. Tip-enhanced nano-Raman analytical imaging of locally induced strain distribution in carbon nanotubes. *Nat. Commun.* **2013**, *4*, 2592.
- (26) Zhong, Q.; Inniss, D.; Kjoller, K.; Elings, V. Fractured polymer/silica fiber surface studied by tapping mode atomic force microscopy. *Surface Science Letters* **1993**, *290*, L688–L692.
- (27) Kurouski, D.; Dazzi, A.; Zenobi, R.; Centrone, A. Infrared and Raman chemical imaging and spectroscopy at the nanoscale. *Chem. Soc. Rev.* **2020**, *49*, 3315–3347.

- (28) Su, W.; Kumar, N.; Krayev, A.; Chaigneau, M. In situ topographical chemical and electrical imaging of carboxyl graphene oxide at the nanoscale. *Nat. Commun.* **2018**, *9*, 2891.
- (29) Budich, C.; Neugebauer, U.; Popp, J.; Deckert, V. Cell wall investigations utilizing tip-enhanced Raman scattering. *J. Microsc.* **2008**, *229*, 533–539.
- (30) Yano, T.-a.; Ichimura, T.; Taguchi, A.; Hayazawa, N.; Verma, P.; Inouye, Y.; Kawata, S. Confinement of enhanced field investigated by tip-sample gap regulation in tapping-mode tip-enhanced Raman microscopy. *Appl. Phys. Lett.* **2007**, *91*, 121101.
- (31) Hermann, P.; Hecker, M.; Chumakov, D.; Weisheit, M.; Rinderknecht, J.; Shelaev, A.; Dorozhkin, P.; Eng, L. M. Imaging and strain analysis of nano-scale SiGe structures by tip-enhanced Raman spectroscopy. *Ultramicroscopy* **2011**, *111*, 1630–1635.
- (32) Marquestaut, N.; Talaga, D.; Servant, L.; Yang, P.; Pauzuskie, P.; Lagugné-Labarthe, F. Imaging of single GaN nanowires by tip-enhanced Raman spectroscopy. *J. Raman Spectrosc.* **2009**, *40*, 1441–1445.
- (33) Ogawa, Y.; Toizumi, T.; Minami, F.; Baranov, A. V. Nanometer-scale mapping of the strain and Ge content of Ge/Si quantum dots using enhanced Raman scattering by the tip of an atomic force microscope. *Phys. Rev. B* **2011**, *83*, No. 081302(R).
- (34) Snitka, V.; Rodriguez, R. D.; Lendraitis, V. Novel gold cantilever for nano-Raman spectroscopy of graphene. *Microelectron. Eng.* **2011**, *88*, 2759–2762.
- (35) Wood, B. R.; Bailo, E.; Khiavi, M. A.; Tilley, L.; Deed, S.; Deckert-Gaudig, T.; McNaughton, D.; Deckert, V. Tip-Enhanced Raman Scattering (TERS) from Hemozoin Crystals within a Sectioned Erythrocyte. *Nano Lett.* **2011**, *11*, 1868–1873.
- (36) Martin, Y.; Williams, C.; Wickramasinghe, H. Atomic force microscope-force mapping and profiling on a sub 100-Å scale. *J. Appl. Phys.* **1987**, *61*, 4723–4729.
- (37) Cleveland, J. P.; Anczykowski, B.; Schmid, A. E.; Elings, V. B. Energy dissipation in tapping-mode atomic force microscopy. *Appl. Phys. Lett.* **1998**, *72*, 2613–2615.
- (38) Saunin, S. A.; Krayev, A. V.; Zhishimontov, V. V.; Gavrilyuk, V. V.; Grigorov, L. N.; Belyaev, A. V.; Evplov, D. A. Systems and devices for non-destructive surface chemical analysis of samples. 2018; US9910066B2.
- (39) Paulo, A. S.; García, R. Tip-surface forces, amplitude, and energy dissipation in amplitude-modulation (tapping mode) force microscopy. *Phys. Rev. B* **2001**, *64*, 193411.
- (40) García, R.; San Paulo, A. Attractive and repulsive tip-sample interaction regimes in tapping-mode atomic force microscopy. *Phys. Rev. B* **1999**, *60*, 4961–4967.
- (41) Dobrzańska-Danikiewicz, A. D.; Łukowiec, D.; Cichocki, D.; Wolany, W. Carbon nanotubes manufacturing using the CVD equipment against the background of other methods. *Archives of Materials Science and Engineering* **2013**, *64* (2), 103–109.
- (42) Taguchi, A.; Yu, J.; Verma, P.; Kawata, S. Optical antennas with multiple plasmonic nanoparticles for tip-enhanced Raman microscopy. *Nanoscale* **2015**, *7*, 17424–17433.
- (43) McCourt, L. R.; Ruppert, M. G.; Routley, B. S.; Indirathankam, S. C.; Fleming, A. F. A comparison of gold and silver nanocones and geometry optimization for tip-enhanced microscopy. *J. Raman Spectrosc.* **2020**, *51*, 2208–2216.
- (44) McCourt, L. R.; Routley, B. S.; Ruppert, M. G.; Keast, V. J.; Sathish, C.; Borah, R.; Goreham, R. V.; Fleming, A. J. Single-Walled Carbon Nanotubes as One-Dimensional Scattering Surfaces for Measuring Point Spread Functions and Performance of Tip-Enhanced Raman Spectroscopy Probes. *ACS Applied Nano Materials* **2022**, *5*, 9024–9033.
- (45) McCourt, L. R.; Routley, B. S.; Ruppert, M. G.; Fleming, A. J. Feasibility of gold nanocones for collocated tip-enhanced Raman spectroscopy and atomic force microscope imaging. *J. Raman Spectrosc.* **2024**, *55*, 336–346.
- (46) Huang, T.-X.; Huang, S.-C.; Li, M.-H.; Zeng, Z.-C.; Wang, X.; Ren, B. Tip-enhanced Raman spectroscopy: tip-related issues. *Anal. Bioanal. Chem.* **2015**, *407*, 8177–8195.
- (47) Meng, L.; Huang, T.; Wang, X.; Chen, S.; Yang, Z.; Ren, B. Gold-coated AFM tips for tip-enhanced Raman spectroscopy: theoretical calculation and experimental demonstration. *Opt. Express* **2015**, *23*, 13804–13813.
- (48) Miranda, H.; Rabelo, C.; Caçado, L. G.; Vasconcelos, T. L.; Oliveira, B. S.; Schulz, F.; Lange, H.; Reich, S.; Kusch, P.; Jorio, A. Impact of substrate on tip-enhanced Raman spectroscopy: A comparison between field-distribution simulations and graphene measurements. *Physical Review Research* **2020**, *2*, 023408.
- (49) Kurouski, D. Advances of tip-enhanced Raman spectroscopy (TERS) in electrochemistry, biochemistry, and surface science. *Vib. Spectrosc.* **2017**, *91*, 3–15.
- (50) Huang, T.-X.; Huang, S.-C.; Li, M.-H.; Zeng, Z.-C.; Wang, X.; Ren, B. Tip-enhanced Raman spectroscopy: tip-related issues. *Anal. Bioanal. Chem.* **2015**, *407*, 8177–8195.

Supplementary Material for
Modulated-Illumination Intermittent-Contact
Tip-Enhanced Raman Spectroscopy

Michael G. Ruppert,^{*,†} Ben S. Routley,[‡] Luke R. McCourt,[‡] Yuen K. Yong,[‡] and
Andrew J. Fleming[‡]

*†University of Technology Sydney, Centre for Audio, Acoustics and Vibration, Ultimo,
NSW 2007, Australia*

‡The University of Newcastle, Callaghan NSW 2308, Australia

E-mail: michael.ruppert@uts.edu.au

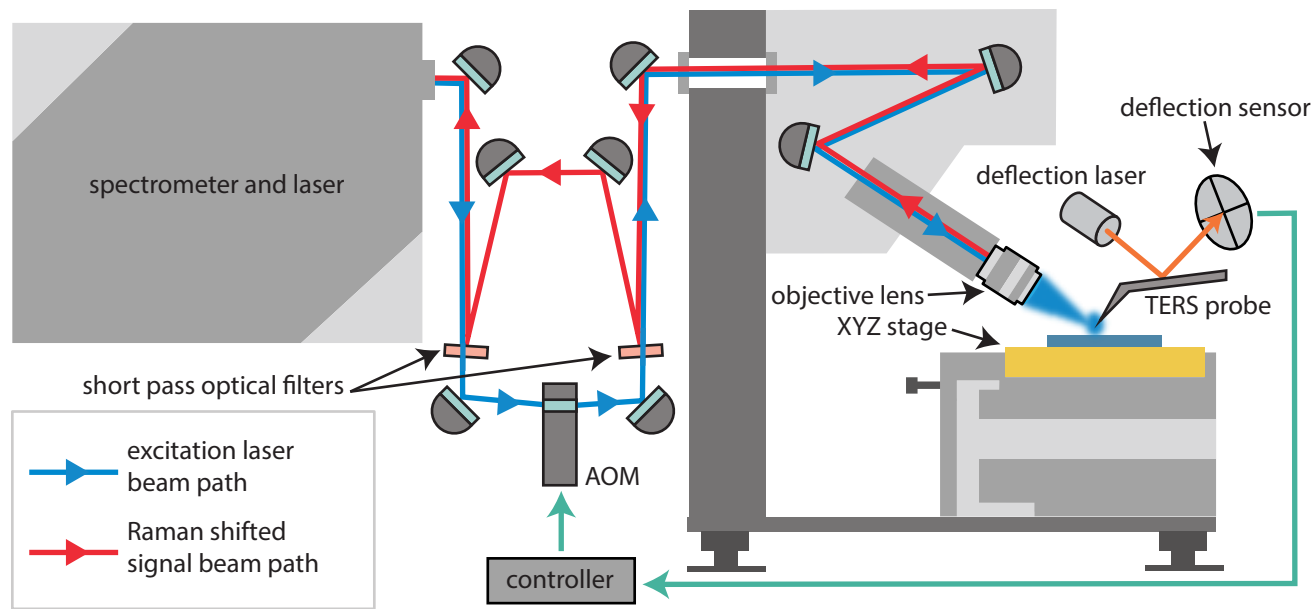


Figure S1: Schematic of the MIIC-TERS experimental setup highlighting the key components.

Experimental Setup

The experimental setup is based on a Horiba XploRA-AFM TERS microscope. This microscope uses the side illumination and collection configuration. A 100X Mitutoyo objective lens with a NA of 0.7 focuses the excitation beam on to the TERS probe; this lens is housed in a nanopositioner allowing for precise alignment. An acoustic optical modulator (AOM) (Isomet IMAD-P80L-1.5) modulates the illumination source. The AOM is introduced to the input beam path via two optical edge filters (Semrock 638 nm short pass), which also divert the output beam around the AOM, as shown schematically in Figure S1. To accommodate the additional optical components and their associated alignment mirrors and opto-mechanical components, an external optical breadboard was installed. To insert this external configuration into the pre-existing optical beam path, two bypass mirrors were inserted between the laser and spectrometer and the AFM. The illumination wavelength used was 638 nm, and the power was set to $200 \mu\text{W}$.

For all AFM-TERS measurements, a Horiba Raman test sample with single-walled carbon nanotubes (CNTs) and graphene oxide flakes dispersed on a 100 nm gold layer on glass

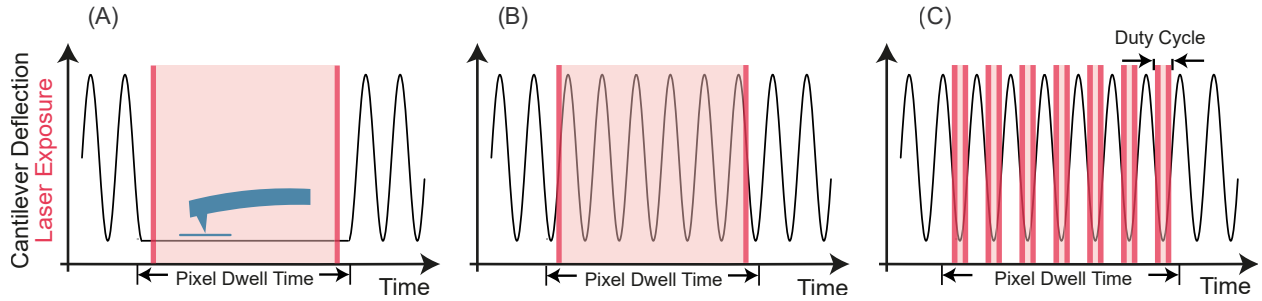


Figure S2: Illustrative timing diagram between cantilever oscillation and Raman laser exposure for (A) hybrid mode TERS, (B) CIIC-TERS, and (C) MIIC-TERS.

was imaged with a silver-coated OmniTM TERS probe from Horiba Scientific (OMNI-TERS-FM-Ag). The cantilever has a nominal spring constant of 2.7 N/m, nominal resonance frequency of 60 kHz, and tip radius of 200 nm. The tapping amplitude was set to 20 nm for all measurements.

Scanning Protocols

Hybrid Mode TERS

The images presented in Figure 3 (A)-(B) of the main manuscript were obtained with the factory standard Horiba Scientific hybrid scanning protocol (SpecTopTM)¹ which bypass the components of the MIIC-TERS setup. In this mode, topography images are obtained in amplitude-modulation intermittent-contact mode and Raman spectra are obtained at each pixel by performing a to-contact approach to a desired force set point. Typical interaction forces are in the order of 2 – 10 nN with an Raman laser exposure time of 0.05 – 0.5 s.¹ The transition between acquisition of topography and Raman spectrum results in a discontinuous scanning trajectory since the cantilever repeatedly switches between amplitude modulation (to acquire topography) and contact mode (to acquire Raman spectrum). This process is illustrated in FigureS2(A). Note that the pixel dwell time is longer than the laser exposure time to accommodate for the tip-sample approach and settling of the cantilever dynamics, which leads to increased imaging time. All imaging parameters are summarized in TableS1.

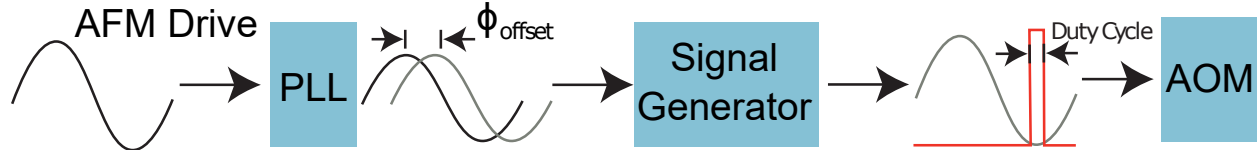


Figure S3: Schematic block diagram of the MIIC-TERS setup.

Constant Illumination Intermittent Contact TERS (CIIC-TERS)

The images presented Figure 3 (C)-(D) of the main manuscript were obtained in constant-amplitude intermittent-contact mode with constant laser illumination and continuous scanning. Since the cantilever position with respect to the sample is not synchronized with the Raman spectrum acquisition, a large amount of background scatter is captured. This process is illustrated in Figure S2(B). All imaging parameters are summarized in Table S1.

Modulated-Illumination Intermittent-Contact TERS (MIIC-TERS)

The imaging results presented in Figure 5 (A)-(D) of the main manuscript were obtained with Modulated-Illumination Intermittent-Contact TERS (MIIC-TERS). A suitable illumination duty cycle for the sample and AFM configuration was found by tuning the Raman spectra from a graphene flake as a known sample. Initially, the duty cycle was set to 25%, and the phase was swept until a Raman spectrum typical for a graphene flake was observed. The laser pulse duty cycle was then slightly reduced, and the phase was once again swept to maximize the graphene flake spectrum. This process was repeated until there was a reduction in the best achievable graphene flake spectrum amplitude, which corresponded to a duty cycle of approximately 5%. A timing diagram for the laser modulator and oscillation cycle is shown in Figure S2(C); and a block diagram of the MIIC-TERS setup is shown in Figure S3. A phase-locked loop (PLL) is used to generate a phase-shifted signal with respect to the AFM cantilever drive to accommodate for the cantilever dynamics. A signal generator is subsequently used to create a square-wave signal with a defined duty cycle to modulate the acoustic optical modulator (AOM) acting on the Raman illumination laser. All imaging

parameters are summarized in Table S1.

Imaging Parameters

The imaging parameters for the results presented in Figure 3(A)-(D) and Figure 5 (A)-(D) of the main manuscript are summarized in Table S1. The amplitude setpoint has been optimized for each imaging mode following best practices.

Table S1: Imaging Parameters for the results presented in Figure 3(A)-(D) and Figure 5 (A)-(D) of the main manuscript.

Parameter	Value		
	Hybrid Mode TERS	CIIC-TERS	MIIC-TERS
Image Size	$5 \times 5 \mu\text{m}$	$5 \times 5 \mu\text{m}$	$1 \times 1 \mu\text{m}$
Image Resolution	100×100 pixel		
Pixel Size	50 nm	50 nm	10 nm
Free-air Amplitude	20 nm		
Amplitude Setpoint	55%	35%	46%
Exposure Time	500 ms		
Imaging Time	117 min	100 min	100 min
Pixel Dwell Time	700 ms	600 ms	600 ms

Image Post-processing

Topography images have been post-processed by removing a background plane due to slight sample tilt. Additionally, a slow drift in the optical components was observed which leads to a drift in sensitivity in the direction of the slow-scan axis in the Raman maps shown in Figure 5 (A)-(C) of the main manuscript. This artifact was removed by estimating the background Raman spectrum for each point of the map with the use of linear interpolation and excluding the D-, G- and 2D-bands. The boundaries of the bands were defined to be $1200 - 1400 \text{ cm}^{-1}$, $1500 - 1700 \text{ cm}^{-1}$ and $2500 - 2700 \text{ cm}^{-1}$ for the D-, G- and 2D-bands, respectively. This estimated background Raman spectrum was removed from the spectra,

and the Raman signal was summed between the boundaries of each band. No other spatial filtering was applied to the images.

Numerical Results

The intermittent-contact TERS imaging results with constant and modulated illumination are further corroborated with Matlab simulations using the metallic nanoparticle boundary element method (MPNBEM)² combined with a time-domain intermittent-contact AFM simulation. First, a single mode of the cantilever interacting with a gold sample is simulated by solving

$$\ddot{y}(t) + \frac{\omega_0}{Q}\dot{y}(t) + \omega_0^2 y(t) = u(t) \quad (1)$$

with

$$u(t) = \frac{\omega_0^2}{k} [F_d \sin(\omega_0 t) + F_{ts}(d, t)] \quad (2)$$

being the input force and d, Q, ω_0, k, F_d are the tip-sample separation, quality factor, resonance frequency, stiffness, drive force amplitude and $F_{ts}(d, t)$ is the tip-sample force as a function of tip-sample distance. Here, the Derjaguin-Muller-Toporov (DMT) model³ is used for the tip-sample interaction which combines classical Hertz contact mechanics with van der Waals forces to model the attractive forces between stiff samples with low adhesion.⁴ The simulations resulted in repulsive interaction for amplitude set points of 75%, 55%, 35% and attractive interaction for 95% amplitude set point. The parameters given in Table S2 are adapted from published data⁵ for the probe and sample used in this simulation.

The resulting cantilever tip trajectories are then used to solve Maxwell's equations for isotropic metallic nanoparticles at optical wavelengths. For this purpose, the simulation toolbox MNPBEM² for metallic nanoparticles (MNP) based on a boundary element method

Table S2: Summary of dynamic AFM simulation parameters.

Param.	Description	Value
A_0	free-air amplitude	30 nm
Q	Q factor	200
k	stiffness	10 N/m
F_d	drive force amplitude	$\frac{kA_0}{Q}$
ω_0	resonance frequency	$2\pi 60$ kHz
SP	setpoint	[35 % – 95 %]
H	Hamaker constant	$7.1e^{-20}$ J
R	tip radius	200 nm
a_0	atomic separation	0.164 nm
E_t	elastic modulus tip	130 GPa
ν_t	Poisson ratio tip	0.3
E_s	elastic modulus sample	80 GPa
ν_s	Poisson ratio sample	0.3

(BEM) approach^{6,7} is employed. The boundary element method allows the plasmon response of metallic nanoparticles to be calculated at optical excitation wavelengths. These calculations solve a set of six equations based on the full set of frequency domain Maxwell's equations to yield the surface charge of the nanoparticle. From the surface charge, the electric field enhancement surrounding the particle can be found. For the full set of equations, the reader is referred to previously published work.^{2,8} The simulation results are consistent with analytic solutions for spheres and ellipsoids.⁹ The method was used to calculate the electric field enhancement surrounding a silver nanocone with a 1 μm length, 200 nm radius of curvature and 15° half-angle (approximating the experimental AFM probe) for a range of tip-sample distances. A 635 nm plane-wave with a linear polarization aligned with the nanocone major axis was used as the illumination source. An exponential model of the form $f(x) = ae^{bx} + ce^{dx}$ was fitted to the numerical results using least-squared regression where x is the tip-sample separation and $f(x)$ is the enhancement; the model is plotted in Figure

4(A) of the main manuscript. The coefficients with 95% confidence intervals are

$$a = 42.7 \quad (1.009, 84.39) \quad (3)$$

$$b = -0.2108 \quad (-0.6054, 0.1838) \quad (4)$$

$$c = 16.65 \quad (-35.46, 68.77) \quad (5)$$

$$d = -0.0337 \quad (-0.1324, 0.065). \quad (6)$$

The average tip-sample force \bar{F}_{ts} is found by applying energy conservation principles and the virial theorem¹⁰ which results in

$$\bar{F}_{ts} = \frac{A_0 k}{2Q} \sqrt{1 - SP^2} \quad (7)$$

where A_0 is the free-air amplitude and $SP = A/A_0$ is the amplitude set point. This formula was shown to be a valid approximation for stiff samples and tip-sample distances where the contact time is less than $0.2/f_0$ (i.e. set points higher than 20%).¹⁰

Discussion on Shadowing Artifact

The topography map in Figure 5(D) in the main manuscript reveals two large round features in the top-right and lower-left corner which are not represented in the corresponding TERS images. These are labeled as features 1 and 2 in Figure S4(A) and (C). In particular, feature 2 shadows feature 3. Since these features do not exhibit any significant Raman spectra in Figure S4(B), they are assumed to be sample contamination which introduces an approximately 12 nm offset between the TERS probe tip and sample surface, which results in suppression of feature 3. The effect of increased tip-sample separation is plotted in Figure 4(A) in the main manuscript, which shows that a 12 nm increase in separation can result in a significant intensity reduction. This phenomenon is exacerbated by the large probe radius and lack of correlation between the optical and mechanical centers, which can result in the probe

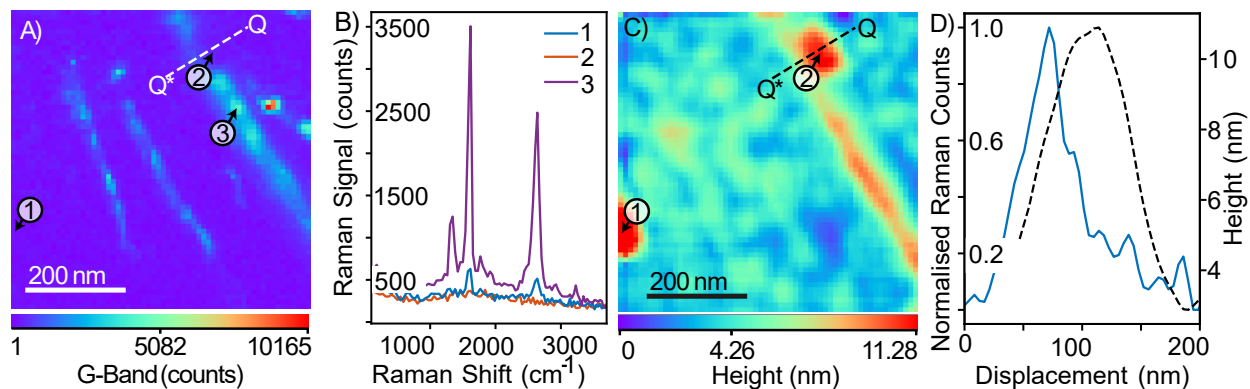


Figure S4: (A) G-band (1580 cm^{-1}) Raman map, (B) Raman D-, 2D- and G-bands for the features labeled 1, 2, and 3 in (A), (C) intermittent contact AFM height map, and (D) Raman G-band and height for the cross section Q*-Q highlighted in (A),(C). Imaging parameters: Free-air amplitude 20 nm; amplitude setpoint 46%; image size $1 \times 1\ \mu\text{m}$, 100×100 pixel; pixel dwell time 600 ms; exposure time 500 ms; duty cycle 5%; imaging time 100 min.

‘riding-up’ high-profile parts of the sample without illuminating the feature underneath it.¹¹

Figure S4(D) shows a cross-section along the line Q*-Q highlighted in Figure S4(A) and (C).

It can be observed that the Raman intensity drops off sharply at the onset of feature 2.

References

- (1) Su, W.; Kumar, N.; Krayev, A.; Chaigneau, M. In situ topographical chemical and electrical imaging of carboxyl graphene oxide at the nanoscale. *Nature communications* **2018**, *9*, 2891.
- (2) Hohenester, U.; Trügler, A. MNPBEM – A Matlab toolbox for the simulation of plasmonic nanoparticles. *Computer Physics Communications* **2012**, *183*, 370 – 381.
- (3) Derjaguin, B.; Muller, V.; Toporov, Y. Effect of contact deformations on the adhesion of particles. *Journal of Colloid and Interface Science* **1975**, *53*, 314 – 326.
- (4) Butt, H.-J.; Cappella, B.; Kappl, M. Force measurements with the atomic force microscope: Technique, interpretation and applications. *Surface Science Reports* **2005**, *59*, 1–152.

- (5) Kiracofe, D.; Melcher, J.; Raman, A. Gaining insight into the physics of dynamic atomic force microscopy in complex environments using the VEDA simulator. *Review of Scientific Instruments* **2012**, *83*, 013702.
- (6) De Abajo, F. G.; Howie, A. Retarded field calculation of electron energy loss in inhomogeneous dielectrics. *Physical Review B* **2002**, *65*, 115418.
- (7) De Abajo, F. G. Optical excitations in electron microscopy. *Reviews of modern physics* **2010**, *82*, 209.
- (8) Waxenegger, J.; Trügler, A.; Hohenester, U. Plasmonics simulations with the MNPBEM toolbox: Consideration of substrates and layer structures. *Computer Physics Communications* **2015**, *193*, 138–150.
- (9) Hohenester, U. Simulating electron energy loss spectroscopy with the MNPBEM toolbox. *Computer Physics Communications* **2014**, *185*, 1177–1187.
- (10) Paulo, A. S.; García, R. Tip-surface forces, amplitude, and energy dissipation in amplitude-modulation (tapping mode) force microscopy. *Phys. Rev. B* **2001**, *64*, 193411.
- (11) McCourt, L. R.; Routley, B. S.; Ruppert, M. G.; Fleming, A. J. Feasibility of gold nanocones for collocated tip-enhanced Raman spectroscopy and atomic force microscope imaging. *Journal of Raman Spectroscopy* **2024**, *55*, 336–346.